

A Theoretical Method for Computing Near-Fault Ground Motions in Layered Half-Spaces Considering Static Offset Due to Surface Faulting, with a Physical Interpretation of Fling Step and Rupture Directivity

by Yoshiaki Hisada and Jacobo Bielak

Abstract An efficient mathematical method is presented for computing the near-fault strong ground motions in a layered half-space, giving explicit consideration to the static offset due to surface faulting. In addition, the combined effects of “fling step” and “rupture directivity” on the near-fault ground motions are investigated. First, after checking the fault integration in the representation theorem, it is found that when an observation point is close to the fault plane, Green’s functions exhibit near singularities, which consist of extremely sharp peaks in a narrow band close to the observation point. Therefore, direct numerical integration becomes quite onerous for computing near-fault ground motions, because the dynamic Green’s functions must then be distributed very densely in order to evaluate accurately the effects of the near singularities. Instead, a new form of the representation theorem is introduced, which exploits the property that the dynamic Green’s functions can be approximated by the corresponding static Green’s functions in the vicinity of the singularities. The modified theorem, which involves the device of adding and subtracting the static Green’s functions from the dynamic ones, is the sum of two fault integrations. The first integration involves the difference of the dynamic and the corresponding static Green’s functions, while the second contains only the static Green’s functions. This formulation requires much less CPU time than the original one when near-fault ground motions are considered, because the near singularities of the dynamic Green’s functions in the first integration are completely eliminated by subtracting the static Green’s functions. While the second integration does require a densely distributed set of points to capture the near-singular behavior of the static Green’s function, it needs to be performed only once, as it is valid for all frequencies. Subtraction of the static Green’s functions from the dynamic functions has the added benefit of making the integration over the wavenumber in the determination of the Green’s functions much more efficient, especially for surface faulting. This is because the difference of the dynamic and static integrands converges rapidly to zero with increasing wavenumbers, whereas the original integrands diverge in the case of a source point on the free surface.

The proposed methodology is used to investigate the two most important effects in near-fault ground motions, fling step (e.g., Abrahamson, 2001) and rupture directivity (e.g., Somerville *et al.*, 1997), by paying special attention to the contribution of static and dynamic Green’s functions. It is found that the fling effects stem mainly from the second integral in the modified representation theorem, which involves the static Green’s function. The fling effects are dominant in the slip direction only in the vicinity of the surface fault and are negligible for buried faults, because the static Green’s function attenuates rapidly with distance from the fault, r , as the order of $(1/r^2)$. Also, more importantly, when an observation point is located above a buried fault, the medium has to remain continuous, and thus cannot “fling.” By contrast, the directivity effects stem mainly from the first integral, which involves the dynamic Green’s function, and attenuate much more slowly than the fling, on the order from $1/r$ to $1/\sqrt{r}$. The directivity effects are dominant in the fault-normal direction, especially

in the forward rupture direction, not only for the surface fault, but also for the buried fault. Due to the combined effects of fling and directivity in the vicinity of the surface fault, the directions of the maximum velocities and displacements are inclined with respect to the fault plane. On the other hand, when softer surface layers are added to the medium, the directivity effects become more significant than the fling effects, because the dynamic Green's functions are more pronounced than the static ones.

Introduction

Recent large-scale inland earthquakes, especially the 1999 Chi-Chi earthquake of Taiwan and the 1999 Kocaeli earthquake of Turkey, dramatically demonstrated the strong effects of surface faulting on near-fault ground motions (e.g., Shin and Teng, 2001). The effects of surface faulting due to tectonic deformations have been recently called "fling step" (e.g., Abrahamson, 2001). In contrast to "rupture directivity" effects, which show the long-period pulses in the direction normal to the fault plane (e.g., Aki, 1968; Archuleta and Hartzell, 1981; Somerville *et al.*, 1997), the fling effects exhibit long-period pulses and permanent static offsets in the direction of the fault slip. In particular, when the fault rupture reaches the free surface, the faulting slip and the subsequent ground motions are strongly amplified (e.g., Archuleta and Frazier, 1978). Thus, the combination of fling and directivity can have destructive effects on various lifeline facilities and long-period structures, such as high-rise or base-isolated buildings, in the vicinity of the surface fault.

As an example, Figure 1a,b shows the location of the surface faults of the 1992 Landers earthquake and the strong motion at a station in the Lucerne Valley. The station is located in the vicinity of the surface fault (about 2 km away; e.g., Chen, 1995) and in the forward direction of the fault rupture. Figure 1c,d shows the fault-normal and -parallel components of the observed velocity and displacement, respectively. The records clearly show the "forward directivity pulse" in the fault-normal component (i.e., the long-period pulse in velocity and the smaller static offset in displacement) and also the fling step in the parallel component (i.e., the long-period pulse in velocity and the large static offset in displacement). Interestingly, because of the combined effects of directivity and fling, the directions of the maximum velocity and displacement are inclined to the surface fault at about 45°, as shown in Figure 1b.

In this article, we propose an efficient method for simulating these near-fault ground motions using an extended kinematic source. Even though various numerical methods have been available to reproduce the near-fault ground motions considering the surface faulting (e.g., Archuleta and Frazier, 1978; Oglesby and Day, 2001; Ramancharla and Meguro, 2001), analytical methods based on the representation theorem remain a useful and powerful tool. As far as the analytical Green's functions are concerned, earlier studies used to assume simple media, such as the homogeneous full-space (e.g., Aki, 1968; Haskell, 1969) or the homoge-

neous half-space (Kawasaki *et al.*, 1973; Kawasaki, 1975; Anderson, 1976; Levy and Mal, 1976). Nowadays, one can readily obtain those of flat-layered half-spaces (e.g., Bouchon, 1979; Apsel and Luco, 1983; Luco and Apsel, 1983; Hisada, 1993, 1995). However, in order to compute the near-fault ground motions in a layered half-space considering surface faulting accurately, we need to overcome two main obstacles related to the singularity of Green's functions.

We shall first describe these obstacles using the analytical method. The displacement due to a kinematic fault model can be expressed as follows in the frequency domain:

$$U_k(Y; \omega) = \int_{\Sigma} T_{ik}(X, Y; \omega) D_i(X; \omega) d\Sigma, \quad (1)$$

where U_k is the k th component of displacement in the Cartesian coordinate system at an observation point, Y , ω is the circular frequency, X is a source point on the fault plane, and Σ is the fault plane. The T_{ik} is the traction Green's function, and D_i is the i th component of the fault slip; we use the summation convention for subscript i . The Green's function of the layered half-spaces is obtained using the following wavenumber integration:

$$T_{ik}(X, Y; \omega) = \int_0^{\infty} t_{ik}(X, Y; \omega, k) dk, \quad (2)$$

where t_{ik} is the integrand of the traction Green's function. When the observation point is located on the fault plane, the Green's functions become singular as the order of $(1/r^2)$. However, in that case, the fault integration in equation (1) can be evaluated analytically considering Cauchy's principal value if the material is homogeneous, and its value is half of the slip (e.g., Kane, 1994). On the other hand, when the observation point is not on the fault plane but very close to it, Green's functions become nearly singular, that is, their amplitudes show sharp peaks in a narrow area close to the observation point. Therefore, the first obstacle is the need to distribute Green's functions very densely on the area close to the observation point in order to evaluate the fault integration numerically. This means that a large amount of CPU time is required when the dynamic Green's functions of layered half-spaces are used (e.g., Kawasaki, 1975). In addition, when we assume a surface fault, we need to calculate numerous

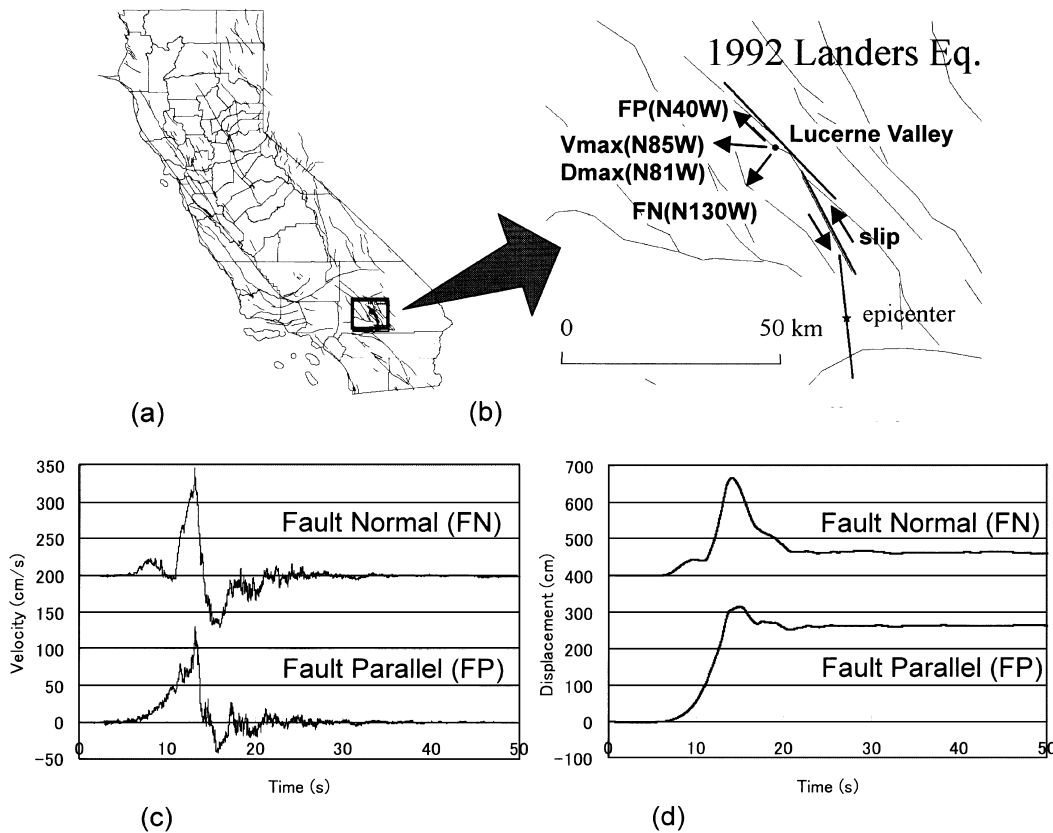


Figure 1. (a) Map of California with the site location; (b) the surface faults and the epicenter of the 1992 Landers earthquake, together with the location of the observation station at the Lucerne valley; (c) the velocities; and (d) the displacements at the station. Panel (b) also shows the direction of the strike slip, the directions of the fault-normal and -parallel components, and the directions of the maximum velocity and displacement.

Green's functions with shallow source points. Therefore, the second obstacle is that the integrands of wavenumber integrations (equation 2) do not converge with wavenumber when the depths of source points are close to or on the free surface (e.g., Apsel and Luco, 1983; Hisada, 1993, 1995). In particular, the convergence is extremely slow in the case of the static Green's function ($\omega = 0$). Therefore, special techniques are needed to overcome the two obstacles.

The purpose of this article is to propose a mathematical methodology for computing near-fault ground motions effectively and to use it for investigating the effects of fling and directivity in several simple situations. We first carefully check the fault integration (equation 1) using the simplest fault model: an axially symmetric circular fault in a homogeneous full-space. Based on the results from this simple case, we will then propose a new form of the representation theorem for calculating the fault integration efficiently for more general cases, involving arbitrary kinematic faulting models in layered half-spaces. In addition, we propose an efficient method for calculating the wavenumber integration (equation 2), considering the surface faulting. Finally, we check the validity of the proposed method and investigate the physical basis of the fling and directivity effects.

Efficient Methods for Computing Near-Fault Ground Motions in Layered Half-Spaces

Near-Fault Ground Motions Using an Axially Symmetric Fault Model in a Homogeneous Full-Space

We first check the basic characteristics of the dynamic and static Green's functions in the fault integration (i.e., equation 1) to find efficient ways for computing the near-fault ground motions. In this section, we use the simplest fault model, that is, the axially symmetric circular fault model in a homogeneous full-space. In addition, we will check the attenuation relation of the static offset using this model.

Figure 2 shows the fault model and the location of an observation point. R is the radius of the circular fault model. We assume a uniform slip, D , over the fault plane. The observation point is located at a distance, z , above the center of the fault. The dynamic displacement, U , in the same direction as D , is easily obtained by substituting Green's function of the homogeneous full-space (e.g., Kane, 1994) into equation (1),

$$U(z, \omega) = \frac{zD}{4} \int_0^R \frac{r}{\zeta^3} \left\{ 2u_1 + u_2 \left(\frac{r}{\zeta} \right)^2 \right\} dr, \quad (3)$$

where D is the fault slip, and

$$\zeta = \sqrt{r^2 + z^2}, \quad (4)$$

$$u_1 = \zeta \chi - r^2 \psi_{, \zeta}, \quad u_2 = 2(\zeta^2 \chi_{, \zeta} - 2\zeta \chi), \quad (5)$$

$$\chi = \left\{ \frac{3}{s^2} - \frac{3}{s} + 1 \right\} \frac{e^s}{\zeta} - \left(\frac{p}{s} \right)^2 \left\{ \frac{3}{p^2} + \frac{3}{p} + 1 \right\} \frac{e^p}{\zeta},$$

$$\chi_{, \zeta} = \left\{ -\frac{9}{s^3} + \frac{9}{s^2} - \frac{4}{s} + 1 \right\} \frac{s}{\zeta^2} e^s - \left(\frac{p}{s} \right)^2 \left\{ -\frac{9}{p^3} + \frac{9}{p^2} - \frac{4}{p} + 1 \right\} \frac{p}{\zeta^2} e^p, \quad (6)$$

$$\psi_{, \zeta} = \left\{ -\frac{3}{s^3} + \frac{3}{s^2} - \frac{2}{s} + 1 \right\} \frac{s}{\zeta^2} e^s - \left(\frac{p}{s} \right)^2 \left\{ -\frac{3}{p^3} + \frac{3}{p^2} + \frac{1}{p} \right\} \frac{p}{\zeta^2} e^p,$$

$$s = i\omega\zeta/V_s, \quad p = i\omega\zeta/V_p. \quad (7)$$

For the static case, equation (3) reduces to

$$U(z) = \frac{zD}{8(1-\nu)} \int_0^R \frac{r}{\zeta^3} \left\{ 2(1-2\nu) + 3\left(\frac{r}{\zeta}\right)^2 \right\} dr, \quad (8)$$

where ν is the Poisson ratio. Note that since the system is axially symmetric, the fault integrations of equations (3) and (8) are one-dimensional along the r axis in the range from 0 to R . When z is directly on the fault (i.e., $z = 0$), the integrals in equations (3) and (8) can be evaluated analytically by using Cauchy's principal values, and their value is half of the slip (e.g., Kane, 1994),

$$U(z = 0, \omega) = \frac{D}{2}. \quad (9)$$

On the other hand, when z is much larger than R , equation (8) can be approximated as

$$U(z) = D \frac{1-2\nu}{8(1-\nu)} \left(\frac{R}{z} \right)^2, \quad (R \ll z). \quad (10)$$

Note that the static displacement attenuates as the inverse of z^2 .

Figure 3 shows the integrands of equations (3) and (8) as a function of r using a fault model with $R = 10$ km and $D = 1$ m for the two cases of (a) $z = 1$ m and (b) $z = 10$ m. The material properties of the medium are $V_s = 3$ km/sec, $V_p = 5$ km/sec, and the corresponding ν is 0.2188. The real parts of the dynamic integrands of equation (3) are plotted in dotted lines for a frequency of 10 Hz, while the static integrands of equation (8) are shown in solid lines. The left figure in Figure 3a shows the integrands from $r = 0$ to 10,000 m for the case of $z = 1$ m. Even though we normalized their amplitudes by their maximum values, these

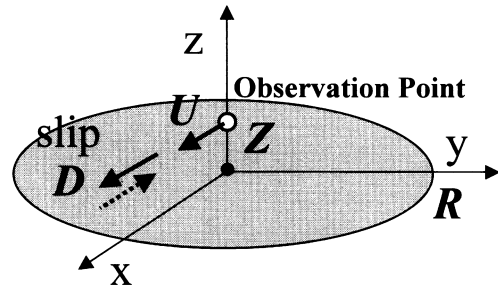


Figure 2. An axial-symmetric fault model in homogeneous full-space. An observation point is located above the center of the circular fault.

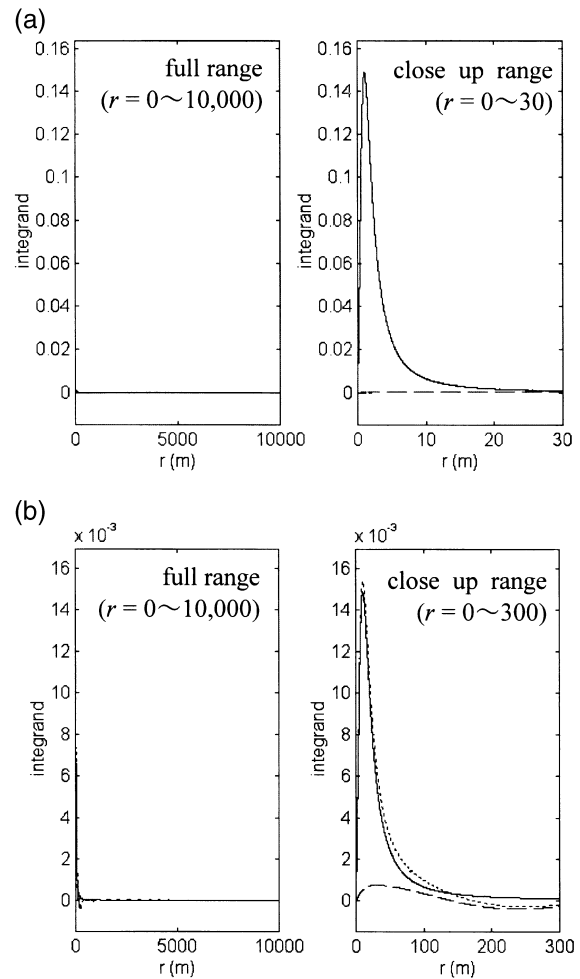


Figure 3. The near-singular behaviors of the integrands of equations (3) and (8) for observation points at (a) $z = 1$ m and (b) $z = 10$ m. The solid and dotted lines are the static and dynamic ($f = 10$ Hz) integrands, respectively, and the dashed line is the value for which the static integrand was subtracted from the dynamic integrand.

amplitudes can barely be seen. The right drawing in Figure 3a shows the same integrand as on the left, except that the integration range has been narrowed to the interval from 0 to 30 m. The spikelike sharp peaks of the integrand then become apparent over an extremely narrow range close to $r = 0$ m and quickly decrease with r . This makes it clear that in order to evaluate the integrals, close attention must be paid to these spikes. Otherwise, the computed amplitude of the displacements near the fault will be in error and far too small. By using a dense distribution of integration points, both equations (3) and (8) give 0.500 m, which is half of the slip, as expected from equation (9). Note that the dynamic integrands in the dotted lines are almost identical to the static ones in the solid lines. Therefore, when we subtract the static integrand from the dynamic integrand, as shown by the dashed line, the values become nearly zero.

Similarly, Figure 3b shows the integrands for $z = 10$ m. The left figure depicts the integrands from $r = 0$ to 10,000 m, and the right is the same integrands except for the range of 0–300 m. Again, the near singularities with sharp peaks occur in both the static and dynamic (10 Hz) integrands in a narrow band around $r = 10$ –30 m. The values of the integrations are 0.499 and 0.489 m for the static and the dynamic cases, respectively. Similarly, since the near singularities are nearly the same for the static and the dynamic cases, the value of their difference becomes a smooth function, with the spike removed, as shown by the dashed line. Therefore, we can eliminate the near singularities of the dynamic integrand by subtracting the static integrand.

Next, we shall evaluate the attenuation of the static displacement. Figure 4 shows the attenuation relations using equations (8) and (10) for the same values of R and D as before (i.e., $R = 10$ km and $D = 1$ m). When z is very close to the fault plane, the value of displacement obtained from equation (8) is about half that of the slip, 0.5 m, as shown in equation (9). The displacement remains nearly constant with z up to about 1 km, around one-tenth of R . It then starts to decrease with increasing z , on the order of $1/z$. Once z exceeds about half the radius, the displacement starts to attenuate as the order of $(1/z^2)$. Therefore, equation (10) then becomes a good approximation, as seen in Figure 4.

An Efficient Method for Computing Near-Fault Ground Motions in a Layered Half-Space

On the basis of the results for the circular fault, we shall propose an efficient method for carrying out the fault integration of the representation theorem for more general cases, that is, arbitrary kinematic faulting models in layered half-spaces. As shown previously, when the observation point is close to the fault plane, the dynamic traction Green's functions exhibit sharp peaks within the area close to the observation point. However, subtracting and adding the static Green's functions can eliminate the singularities of the original Green's function. Thus, we propose the following representation theorem, instead of equation (1):

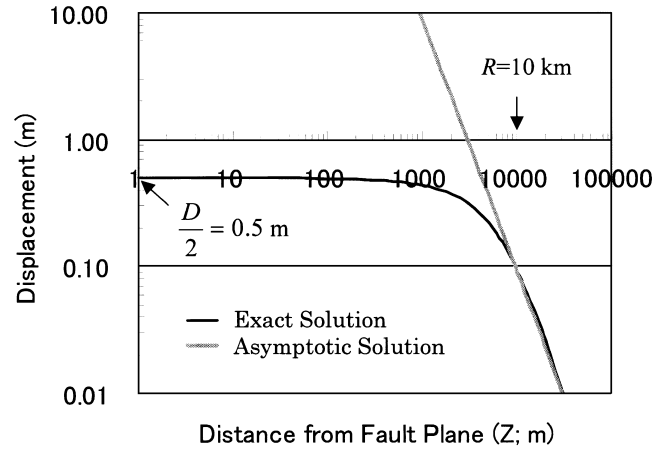


Figure 4. The attenuation relation of the static displacement using a circular fault model with $R = 10$ km and $D = 1$ m in homogeneous full-space. The displacement is nearly constant from 0 to 1 km of z (one-tenth of the fault radius) and attenuates reversely proportionally to the second power of z , when z exceeds about 5 km.

$$U_k(Y; \omega) = \int_{\Sigma} \{T_{ik}(X, Y; \omega) - T_{ik}^S(X, Y)\} D_i(X; \omega) d\Sigma + \int_{\Sigma} T_{ik}^S(X, Y) D_i(X; \omega) d\Sigma, \quad (11)$$

where T_{ik} is the traction Green's function of the layered half-space at circular frequency, ω , and T_{ik}^S is the static traction Green's function of the layered half-space ($\omega = 0$). Addition and subtraction of singular integrands is common when dealing with integral evaluations or integral equations (e.g., Apsel and Luco, 1983; Colton and Kress, 1983; Hisada, 1993, 1995).

Equation (11) consists of two fault integrations. The first integration corresponds to the dynamic Green's function, in which the sharp peak of the original Green's function has been eliminated by the subtraction of the static Green's function. Hence, to evaluate the integral over the fault, we can locate the integration points coarsely at regular grid nodes on the fault plane, even when the observation point is very close to the fault. Also, the first integration indicates that the attenuation of the slip function, D_i , is governed by the dynamic Green's functions, which consist of body and surface waves. Thus, their amplitudes decay on the order of $1/r$ to $1/\sqrt{r}$ (r is the distance from the fault to the observation point).

On the other hand, the second integral in equation (11) involves the static Green's function. To perform this fault integration, we have to distribute the integration points densely in the area close to the observation point in order to incorporate the contribution from the sharp peak. The CPU time required for computing the static function, however, is much less than for the corresponding dynamic function. And more importantly, since the values of the static functions remain invariant for all frequencies, these functions need to

be evaluated only once. The second integral describes the attenuation of the slip function due to the static traction of the Green's functions. Thus, their amplitudes would be expected to decrease rapidly, on the order of $1/r^2$ beyond a certain distance from the fault, as indicated in Figure 4. While we could have chosen some alternative singular functions to remove the singularity from the dynamic Green's function, we have used the static Green's functions both for mathematical convenience and for the physical insight into the fling step and rupture directivity phenomena one gains from their use.

Efficient Methods for Calculating the Dynamic and Static Green's Functions When the Depth of Source Point is Equal or Close to the Depth of Observation Point

Next, we address another problem that arises when one computes the Green's functions of layered half-spaces, considering surface faulting. As mentioned earlier, when the depth of the source is the same as or close to the depth of the observation point, the integrand of the wavenumber integration of equation (2) diverges with increasing wavenumbers. There are several techniques to remedy this problem, both for the dynamic and static cases (see, e.g., Hisada, 1993). We will adopt the most appropriate methods for computing the two integrals in equation (11).

One of the most efficient methods for dealing with the divergent integrand of the dynamic Green's function is to introduce an asymptotic solution of the integrand at large wavenumbers, which is equivalent to the static function. This technique was originally introduced by Apsel and Luco (1983), who used the integrand of the static Green's function of the homogeneous full-space to approximate the dynamic function of layered half-spaces. Later, Hisada (1995) improved the method by introducing an approximate analytical static solution of the layered half-space, which results in a more rapid convergence.

To evaluate the integral of the first integrand of equation (11), we can use the following wavenumber integrations instead of equation (2), since the dynamic Green's functions are already subtracted by the static Green's functions:

$$T_{ik}(X, Y; \omega) - T_{ik}^S(X, Y) = \int_0^\infty \{t_{ik}(X, Y; \omega, k) - t_{ik}^S(X, Y; k)\} dk, \quad (12)$$

where $t_{ik}(X, Y; \omega)$ and $t_{ik}^S(X, Y; \omega)$ are the integrands of the dynamic and static traction Green's functions, respectively. Since the dynamic integrand converges exactly to the static integrand with increasing wavenumber, the integrand of equation (12) attenuates rapidly, even if the depth of the source point is equal to the depth of the observation point. Note that the expression on the right side of equation (12) is of the same form as that used by Apsel and Luco (1983) or Hisada (1993, 1995). However, here we adopt the static

Green's functions of the actual layered system, which guarantee the fastest convergence.

On the other hand, to evaluate the static Green's functions of a layered half-space in the second integration of equation (11), we employ the contour deformation method, which is a well-known technique for evaluating the wavenumber integration efficiently (e.g., Levy and Mal, 1976). Greenfield (1995) applied this technique to evaluate Green's function for the case in which the depth of a source point is close or equal to that of an observation point. This method is more appropriate than the asymptotic method for the static case because the approximate asymptotic solutions, such as the static Green's function of the homogeneous space or Hisada's solution (Hisada, 1995), do not converge efficiently to the integrand of the static Green's function, due to the infinite wavelength. In order to introduce the contour deformation, we first divide the integration range into two parts, as shown in Figure 5,

$$G(z, r) = \int_0^\infty g(z)J(kr)dk = \int_0^{k_A} g(z)J(kr)dk + \int_{k_A}^\infty g(z)J(kr)dk, \quad (13)$$

where $G(z, r)$ is an arbitrary Green's function, z is the depth of the source or observation points, r is the horizontal distance between the source and observation points, $g(z)$ denotes the motion-stress vectors of z (e.g., Aki and Richards, 1980; Hisada, 1993), and $J(kr)$ is the Bessel function of the first kind. The corner wavenumber, k_A , can be arbitrary, but it must be larger than the wavenumbers corresponding to the branch points and the poles in the dynamic case. For the static case, since there are no branch points or poles, an arbitrary small value is possible, such as $k_A r = 1$ or 2.

The second integrand of equation (13) diverges with increasing k when the depths of the source and observation points are close. Thus, we shall introduce the contour deformations (Greenfield, 1995). We first replace the Bessel function by the Hankel functions, as follows:

$$\int_{k_A}^\infty g(z)J(kr)dk = \frac{1}{2} \int_{k_A}^\infty g(z) \{H^{(1)}(kr) + H^{(2)}(kr)\} dk, \quad (14)$$

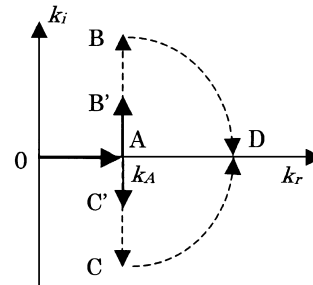


Figure 5. The contour deformation for evaluating the second integration of equation (13), which corresponds to the static Green's function.

where $H^{(1)}$ and $H^{(2)}$ are the Hankel functions of the first and second kinds, respectively. Next, we expand the real wavenumber k to the complex wavenumber and apply Cauchy's theorem. For the integration of $H^{(1)}$, we carry out the contour integration along the contour ABD in Figure 5. The integral on BD vanishes by Jordan's lemma, as k goes to infinity. Moreover, since $H^{(1)}$ decreases exponentially on the path AB, we can terminate the integration on AB at a suitable point B' on that path. Therefore, the integration can be approximated as

$$\int_{kA}^{\infty} g(z)H^{(1)}(kr)dk \approx \int_{AB'} g(z)H^{(1)}(kr)dk_i. \quad (15a)$$

Similarly, we carry out the contour deformation for the integration of $H^{(2)}$ along the contour ACD in Figure 5. We then terminate the integration range at C':

$$\int_{kA}^{\infty} g(z)H^{(2)}(kr)dk \approx \int_{AC'} g(z)H^{(2)}(kr)dk_i. \quad (15b)$$

The numerical integrations in equations (15a) and (15b) can be readily carried out, since both integrands converge quickly to zero with increasing k_i . Therefore, the sum of equations (15a) and (15b) gives accurate values for the second integral of equation (13).

Miscellaneous Techniques for Calculating Strong Motions Including Permanent Offset

We will now provide some additional details on the computation of Green's functions, the numerical integrations, and the calculation of the near-fault ground motions, including static offsets.

Among various available methods for computing the dynamic and static Green's functions of layered half-spaces, we use the method by Hisada (1993), which is modified from Luco and Apsel (1983). This is an appropriate method for this study, as it is completely free from the numerical instabilities at lower and higher frequencies through the introduction of the R/T (reflection/transmission) matrix. In addition, it gives the static solution explicitly (Luco and Apsel, 1983).

For the wavenumber integrations of the dynamic Green's functions in equation (12), which include the poles and the branch points, we use Simpson's and Filon's quadratures for small and large wavenumbers, respectively (Olver, 1964). On the other hand, for the integrations of the static Green's functions in equations (13) and (15), which involve smooth integrands, we use an adaptive Newton-Cotes quadrature.

With regard to the fault integration in equation (11), we divide the fault plane into rectangular subfaults and use Gaussian quadrature in each subfault. For computing the first (dynamic) integration in equation (11), we use a variable number of Gaussian points, up to 6×6 , to keep at least six

points per wavelength. On the other hand, for computing the second (static) integration in equation (11) when an observation point is close to a subfault, we divide the subfault into smaller subfaults and redistribute Gaussian points to evaluate the near-singularity of the static Green's function; we repeat this process until the value of the integration converges within a prescribed tolerance.

The static offset of displacement is calculated as follows. Since the Fourier amplitude of a steplike displacement is infinite at 0 Hz, we first compute velocities in the frequency domain, transforming them into the time domain. Then, we calculate the corresponding displacements by integrating the velocities numerically in the time domain. To check the accuracy of the calculated static offset, we recall that the Fourier amplitude of velocity at 0 Hz is the same as the value of the static offset in the time domain, since the static offset is the displacement as the time goes to infinity.

Numerical Examples

Strike-Slip Model with Surface Faulting in a Homogeneous Half-Space

We shall first check the basic characteristics of the near-fault ground motion using a simple strike-slip model with surface faulting (see Fig. 6). We compute the near-fault ground motions using the proposed representation theorem (equation 11) from 0 Hz up to 10 Hz. As shown in Figure 6a, we use the 12 observation points on the free surface along a line perpendicular to the fault plane. Point 1 is 0.1 km away from the center of the surface fault, and point 2 is 0.5 km away. Similarly, points 3–12 are 1.5–10.5 km away from the fault at 1-km intervals. Because of the symmetry of the model and the pure strike slip, the fault-normal components are zero, and the vertical components are negligible compared to the fault-parallel components. As shown in Figure 6b, the maximum slip of the fault is 1 m, including the shallowest subfaults which break the free surface, and tapers at both edges and at the bottom of the fault. The slip velocity function is an isosceles triangle with a 1-sec duration, as seen in Figure 6c. The rupture velocity is infinite. We use the homogeneous half-space with the physical properties of $\rho = 2.5 \text{ g/cm}^3$, $V_p = 5 \text{ km/sec}$, $V_s = 3 \text{ km/sec}$, $Q_p = 200$, and $Q_s = 100$.

Figure 7 shows the velocities (Fig. 7a) and displacements (Fig. 7b) of the fault-parallel components. Both panels include three sets of waves on the line; the left and middle waveforms correspond to the dynamic and static terms, which stem from the first and second integrals in equation (11), respectively. The rightmost panels represent the sums of the two terms. When observation points are close to the fault (e.g., points 1 and 2), we see the strong fling effects, that is, the large pulse in velocities and the large static offsets in displacement. These consist mainly of static terms, with little contribution from the dynamic terms. Since the static terms decay rapidly with distance from the fault, the fling

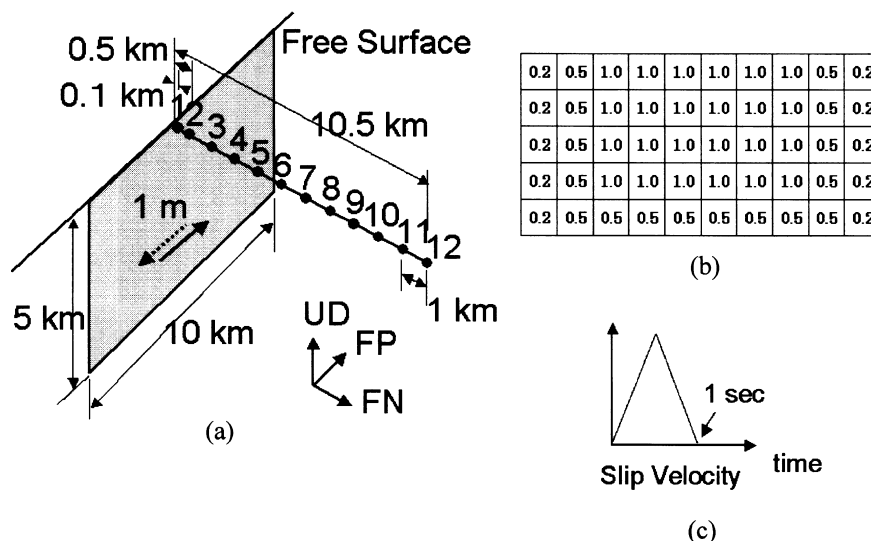


Figure 6. (a) Strike-slip model with surface faulting and 12 observation points; (b) the slip distribution; and (c) the slip velocity function.

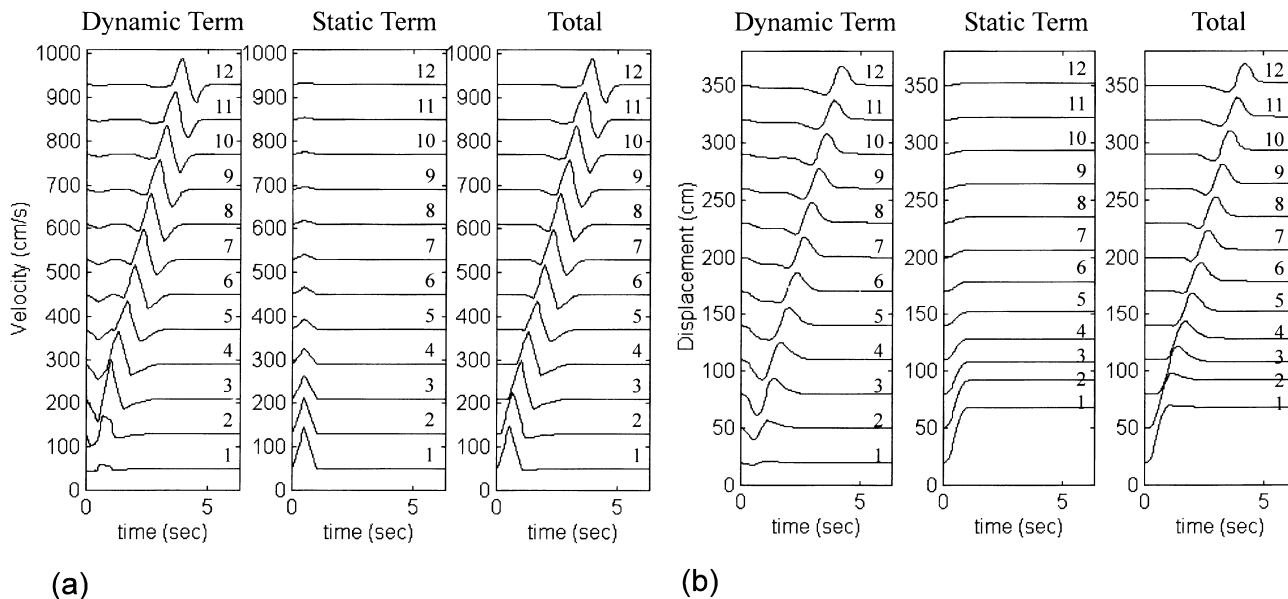


Figure 7. (a) Velocities and (b) displacements of the fault-parallel components at 12 observation points in Figure 6, using the first (dynamic; left), second (static; center), and total (right) integrations of equation (11).

effects disappear for observation points away from the fault (e.g., points 11 and 12). By contrast, the dynamic terms become dominant far from the fault. Note that the static velocities are always isosceles triangles, which correspond to slip velocity function with attenuation (see Fig. 6c).

To check the attenuation relations of the dynamic, static, and total terms with distance, Figure 8 shows the relation between r (the distance from the fault) and the maximum amplitudes of the velocities (Fig. 8a) and displacements (Fig. 8b). In each panel, the thin black lines, the thick gray lines, and the thick black lines correspond to the dynamic,

static, and total terms, respectively. In addition, the dashed line in Figure 8b represents the Fourier amplitudes of velocity at 0 Hz, which agrees with the thick gray line, that is, the values of the static offset. This demonstrates the validity of the results, as explained in the previous section. For small r , the static terms are dominant over the dynamic ones, and the maximum amplitudes are about half of the slip function, that is, 100 cm/sec in velocity and 50 cm in displacement. As the distance becomes large, say, 2–5 km (one-fifth to one-half of the fault dimension), the static terms decrease as $1/r^2$. By contrast, since the dynamic terms are attenuated on

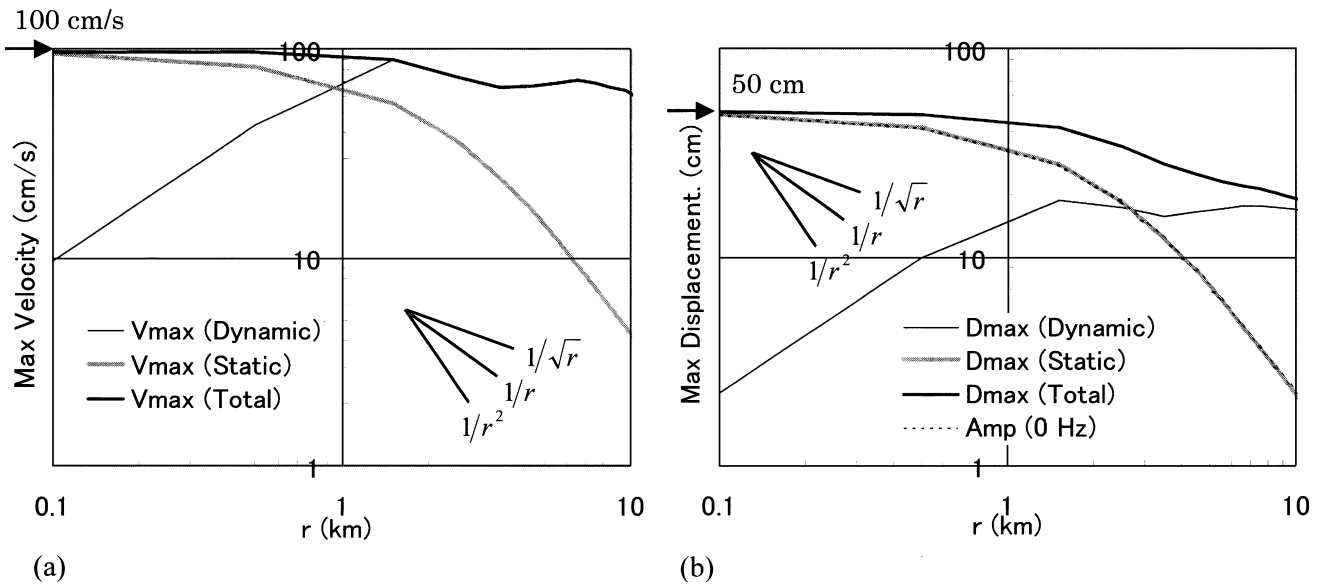


Figure 8. Attenuation relations of the maximum amplitudes in (a) velocities and (b) displacements using the dynamic, static and total waves; 100 cm/sec in velocity and 50 cm in displacement are the half of the slip velocity and the slip. In panel (b), since the maximum displacements of the static terms (i.e., the permanent offsets) and the Fourier amplitudes of velocities at 0 Hz show almost same values, there are no differences in the figure.

the order of $1/r$ to $1/\sqrt{r}$, they become dominant over the static ones at distances greater than 2–5 km. Therefore, the fling effects, which correspond to mostly the static terms, are prominent only in the vicinity of the fault (or asperity size).

Dip-Slip Model with Surface Faulting in a Homogeneous Half-Space

Next, we shall check the near-fault strong motions using a dip-slip model with surface faulting. As shown in Figure 9, the dip and rake angles are 45° and 90° , respectively. The other source and medium parameters are the same as for the previous model (see Fig. 6). We locate 14 observation points on the free surface along the line perpendicular to the fault; points 1–7 are located on the footwall side, and points 8–14 are on the hanging-wall side. The points closest to the fault are points 7 and 8, which are at 0.1 km away from the surface fault trace.

Figure 10a,b shows the fault-normal and up–down components, respectively, of the velocities at the 14 observation points. Similarly, Figure 10c,d shows the corresponding displacements. As in the previous example, the waves in the left and middle panels in each set are the dynamic and static terms, respectively, and the right waves are the sum of the two. Compared with the waves on the footwall (points 1–7), the waves on the hanging wall (points 8–14) show large amplitudes, especially in the up–down components. When observation points are close to the fault, the static terms are dominant over the dynamic ones, and we see strong fling effects. As the observation points get farther from the fault,

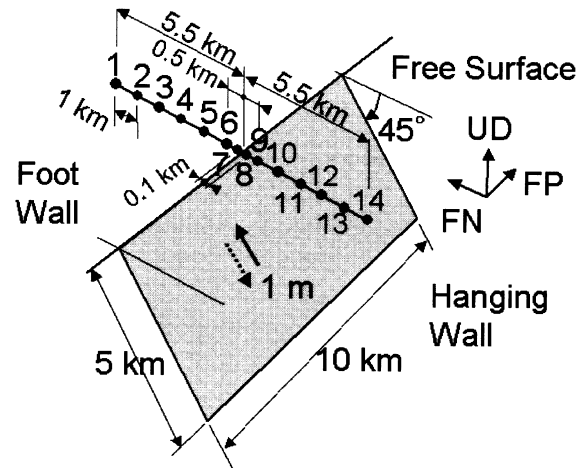


Figure 9. Dip-slip model with surface faulting in homogeneous half-space. The dip angle is 45° , and the other source parameters are the same as Figure 6.

the static terms are quickly attenuated and the dynamic ones become dominant.

Fling versus Directivity Effects Using Surface and Buried Fault Models

We now examine the effects of the fling step and the rupture directivity on the near-fault strong motion for strike-slip models. As shown in Figure 11a,b, we consider both a surface fault model and a buried fault model. As previous studies have indicated, the depth of the top of the fault would

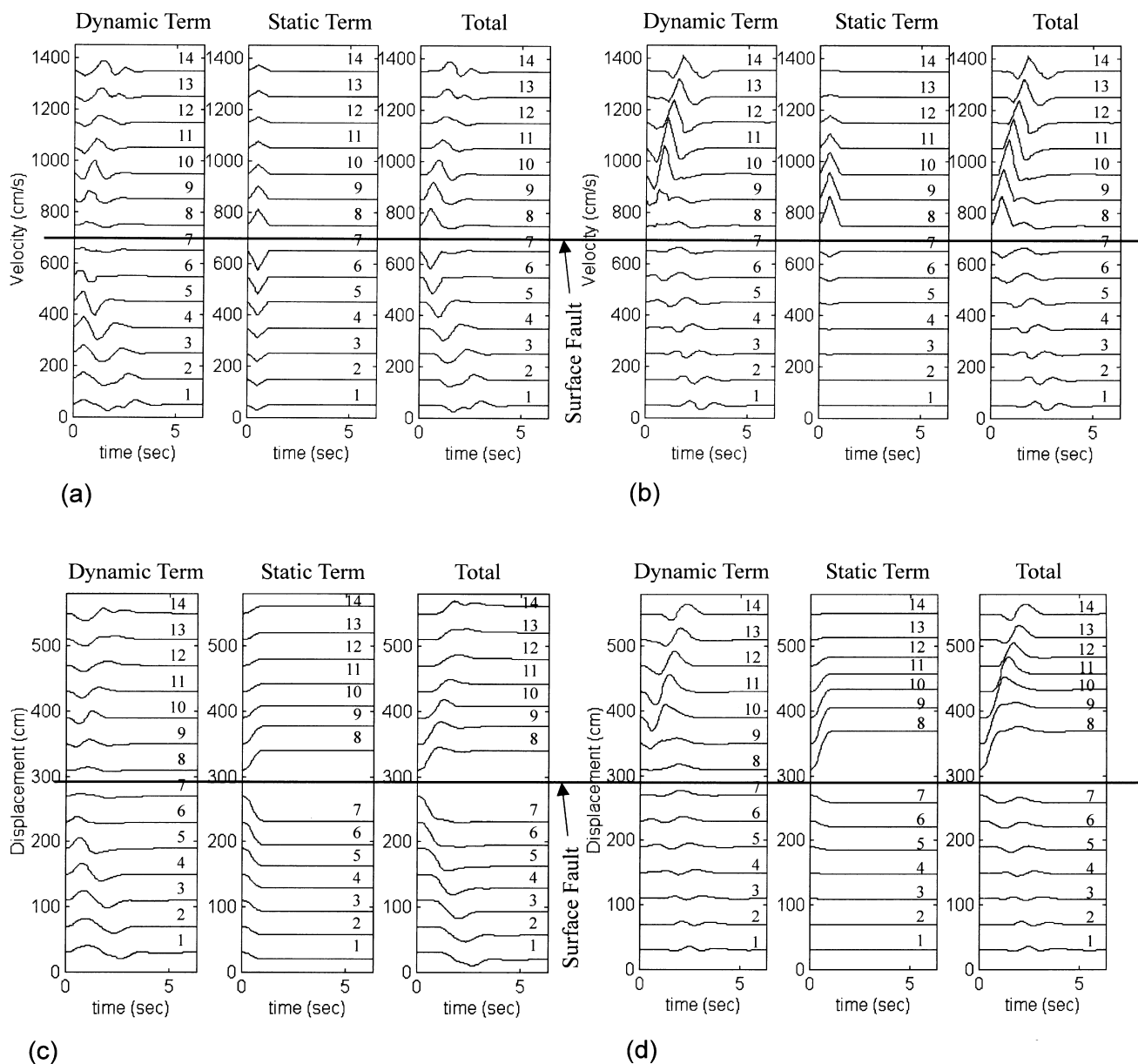


Figure 10. Velocities (a,b) and displacements (c,d) in the fault-normal (a,c) and up-down (b,d) directions at 14 observation points in Figure 9, using the dip-slip model, and the first (dynamic; left), second (static; center), and total (right) integrations of equation (11). The horizontal line indicates the location of the surface fault.

be one of the most important parameters controlling the near-fault ground motions (e.g., Anderson and Luco, 1983a, 1983b; Luco and Anderson, 1983). Most source parameters are the same as in Figure 5, except that now the rupture velocity has a finite value of 2.5 km/sec; this gives rise to directivity effects. The location of the hypocenter is shown in the figure, halfway down the fault. The depth of the top of the buried fault is 2 km, as shown in Figure 11b. We locate 13 observation points at 1-km intervals on the line parallel to the fault plane at a distance of 0.1 km. Thus, observation points 1 and 13 are in the backward and forward directions of the rupture front, respectively.

Figure 12 shows the results of the surface fault model, where panels (a) and (b) are the velocities of the fault-normal and fault-parallel components, respectively, and panels (c) and (d) are the corresponding displacements. As before, the left, middle, and right waves in each figure are the dynamic, static, and total contributions, respectively. In the fault-normal components, we see the growth of the directivity pulses in the forward direction of the rupture front, which consist mostly of the dynamic terms. The contribution of the static terms is minor. By contrast, we see fling waves in the fault-parallel components; these consist of the static terms and are dominant only at the observation points next to the

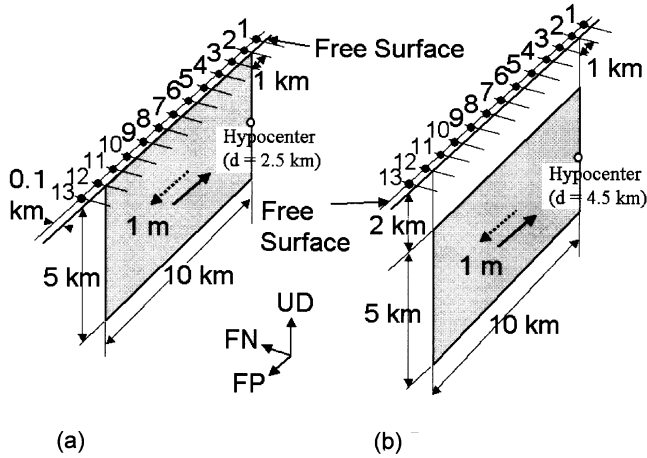


Figure 11. A strike-slip model with (a) surface fault and (b) buried fault in homogeneous half-space. The source parameters are the same as Figure 6, but with $V_r = 2.5$ km/sec.

fault plane (i.e., points 3–11 in Fig. 12). The contributions of the dynamic terms are negligible.

Figure 13a,b depicts the velocities and Figure 13c,d the corresponding displacements for the buried fault model. Notice that the scales of the amplitudes are about half of those in Figure 12. From these figures we can see that the fault-normal components, which are mostly the dynamic waves, exhibit a clear forward directivity effect. On the other hand, the fling waves disappear in this model. As explained before, the fling consists mainly of static Green's functions, which attenuate more quickly than the dynamic ones. And, more importantly, when an observation point is located next to a surface fault, the slip dislocation directly "flings" the adjacent ground in the slip direction. However, when an observation point is located above a buried fault, the slip dislocation cannot fling the ground, because the medium is continuous above the fault.

In order to further illustrate the combined effects of fling and directivity on the near-fault ground motion, Figure 14 shows the vectors of the maximum velocities on the free surface using the surface fault (Fig. 14a) and the buried fault (Fig. 14b), as shown in Figure 11a,b. Again, the amplitude scale for the buried fault is about half of that for the surface fault. In both models, fault-normal components grow in the forward rupture direction (the left side of the figures). In particular, the normal components are dominant in the vicinity of the buried fault. By contrast, we also see large amplitudes in the fault-parallel components near the surface fault in Figure 14a. Therefore, because of the comparable amplitude of fault-parallel and fault-normal components, the directions of the maximum velocities are inclined with respect to the fault plane in the vicinity of the surface fault. In particular, the fault-parallel components are larger than the normal in the area close to the epicenter. As mentioned in the Introduction, the direction of the maximum velocity recorded at Lucerne Valley was inclined to the fault plane (see Fig. 1b). This phenomenon probably occurred by the com-

bined effects of fling and directivity. On the other hand, the fault-normal components become dominant for observation points further away from the surface fault, especially in the forward directivity direction.

Effects of Sedimentary Layers on Near-Fault Ground Motions

Finally, we shall add sedimentary layers to the surface fault model to check the effects of layering on the near-fault ground motions. Table 1 shows the material properties of the layered half-space, in which we have added two sedimentary layers to the homogeneous half-space. We use the same strike-slip model with surface faulting as that shown in Figure 11a. Bouchon (1979) examined the effects of layering using a model with a single layer and a strike-slip fault and found that the amplification was much larger in the fault-normal component than in the parallel-fault component.

Figure 15a,b shows the three components of velocities and displacements, respectively, at the same observation points shown in Figure 11a. Compared with the results of the homogeneous medium shown in the total waves of Figure 12, the fault-normal components show larger amplitudes and longer durations, especially in the forward rupture direction. This is because the fault-normal components are mostly the dynamic terms, that is, the body and surface waves, and they are amplified in the sedimentary layers. For the fault-parallel components, which are represented mostly by the static terms, the waveforms and amplitudes are nearly the same as those of the homogeneous medium.

Concluding Remarks

In this article, we first examined a simple circular fault model (Fig. 2) with the objective of developing efficient methods for computing near-fault strong ground motions. From these simple examples, we have made some important observations. When an observation point is close to the fault plane, the integrands of the fault integrations exhibit near singularities, that is, sharp peaks in the narrow area close to the observation point, as seen in Figure 3. Therefore, in order to obtain accurate values of the integrations without further modification, integration points need to be distributed very densely in the area. However, subtracting the integrand of the static Green's functions can eliminate the near singularity of the dynamic Green's function. We also found that the static displacement (the permanent offset) attenuates rapidly on the order of $1/r^2$ at distances larger than a fraction of the radius R , as shown in Figure 4.

On the basis of these observations, we have proposed a new form of the representation theorem, described by equation (11), from which one can compute the near-fault ground motions in layered half-spaces much more efficiently than with the original equation (equation 1). The proposed theorem entails two fault integrations; the first consists of the difference between the dynamic Green's function and the corresponding static Green's function, and the second consists of the static Green's function. In the first integration,

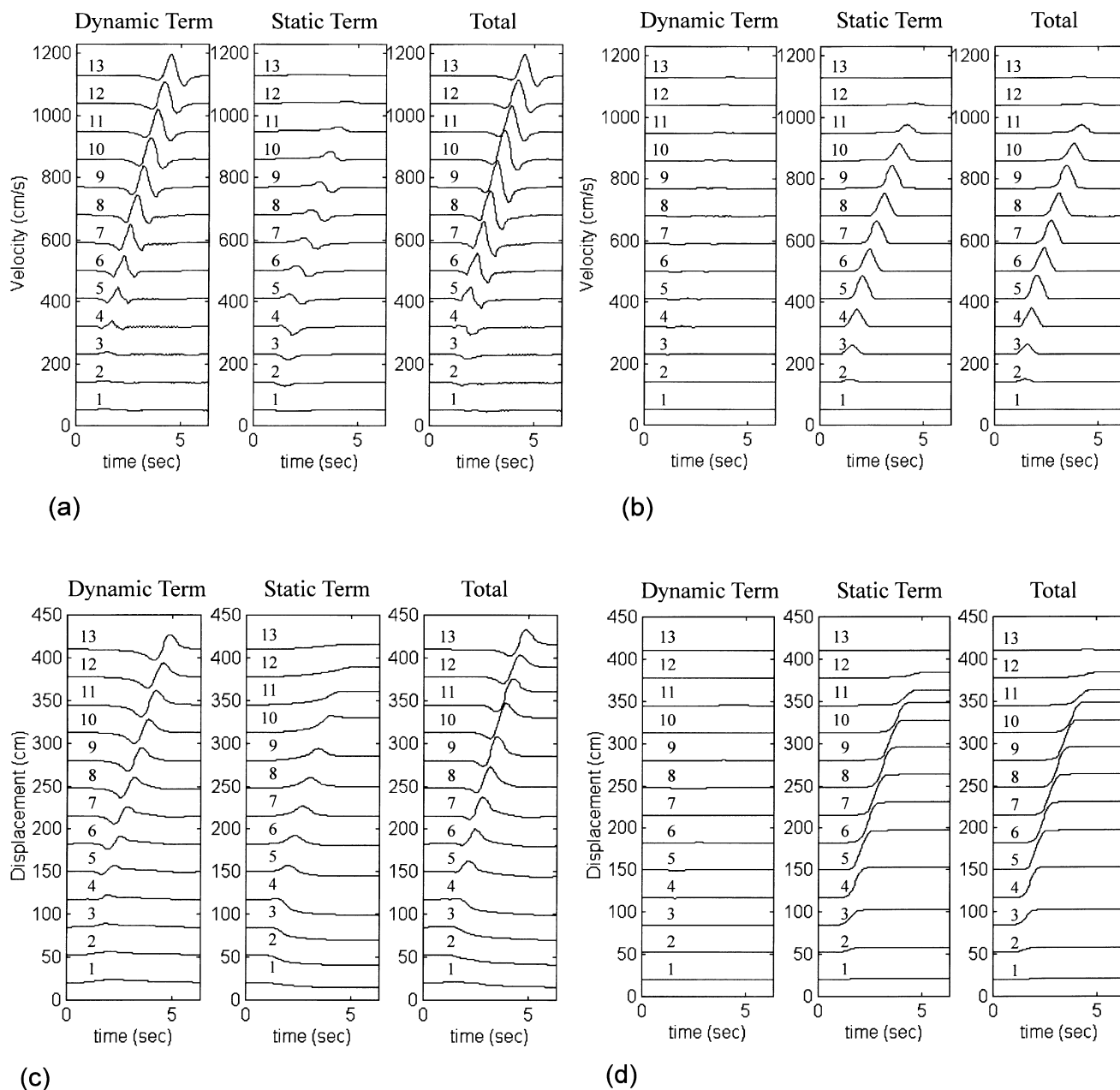


Figure 12. Velocities (a,b) and displacements (c,d) in the fault-normal (a,c) and -parallel (b,d) directions at 13 observation points in Figure 11a, using the first (dynamic; left), second (static; center), and total (right) integrations of equation (11).

the near singularities of the dynamic Green's functions are completely eliminated by the subtraction of the static Green's functions. Therefore, we can carry out numerically the first integration by distributing the integration points on regular grids that consider only the target wavelength. As for the second fault integration, the integration points need to be distributed very densely in the area close to the observation points in order to evaluate the near singularities. However, the required computations are small, because (1) the static Green's functions are much simpler than the corresponding dynamic ones and, more importantly, (2) the computation for the static Green's functions needs to be per-

formed only once; these are then used for all frequencies. It should be noted that the proposed representation theorem is meant to be used only for observation points that are near the fault. Since the near singularities of the dynamic Green's functions disappear as the distance between the observation point and the fault increases, it is unnecessary to introduce the static Green's functions.

We also proposed efficient methods for computing the dynamic and static Green's functions of layered half-spaces in the case of a surface fault. Since the depths of source points are on or close to the free surface in this case, the integrands of the wavenumber integration in equation (2) do

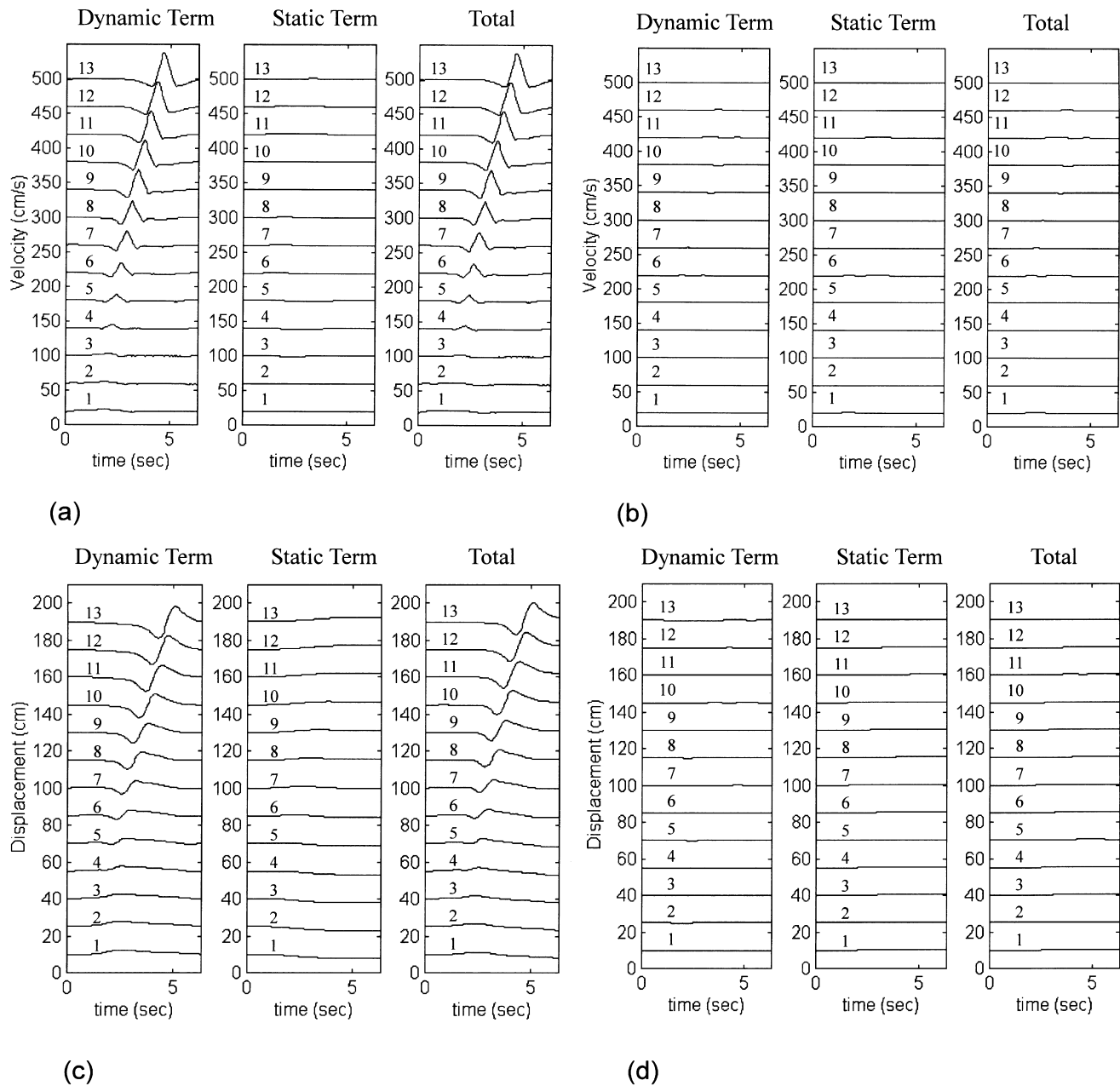


Figure 13. Velocities (a,b) and displacements (c,d) in the fault-normal (a, e) and -parallel (b,d) directions at 13 observation points in Figure 11b, using the first (dynamic; left), second (static; center), and total (right) integrations of equation (11).

not converge. In order to carry out the wavenumber integration of the dynamic Green's function in the first fault integration in equation (11), we use equation (12); its integrand quickly attenuates with the wavenumbers. For the static Green's function of the second fault integration in equation (11), we use the contour deformation method (Greenfield, 1995), as shown in equations (14) and (15). The resulting integrands then have an asymptotic exponential decay and can be easily integrated numerically.

Next, we computed the near-fault ground motions using various idealized models and drew the following conclusions. First, we found that the fling step stems mainly from

the second fault integral in equation (11), which is the convolution of the fault slip and the static traction Green's function. Their amplitudes are dominant in the slip direction in the vicinity of surface faults and are negligible for buried faults. This is because the static Green's function quickly attenuates with distance, on the order of $1/r^2$. In addition, when an observation point is located above a buried fault, the medium has to remain continuous, and thus cannot fling.

On the other hand, we found that the directivity pulse mainly stems from the first integral in equation (11), which is the convolution of the fault slip and the dynamic Green's function. Directivity effects are dominant in the fault-normal

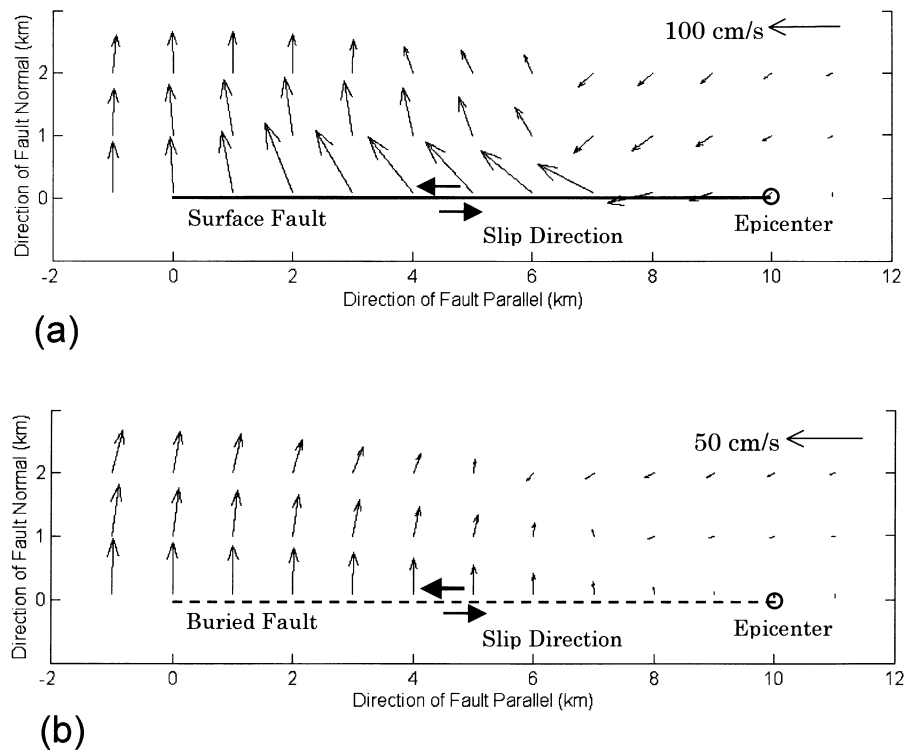


Figure 14. Vectors of maximum velocities on the free surface for the (a) surface and (b) buried faults. In the case of the strike-slip fault, the effects of “fling” and “directivity” can be seen in the components of the fault parallel and the normal, respectively.

Table 1
The Material Properties of the Layered Half-Space

Density (t/m ³)	V _p (km/sec)	V _s (km/sec)	Q _p	Q _s	Thickness (km)
2.2	3.0	1.0	100	50	1
2.4	4.0	2.0	150	75	1
2.5	5.0	3.0	200	100	–

direction, especially in the forward rupture direction, not only for the surface fault, but also for the buried fault. They attenuate much more slowly than the fling, on the order from $1/r$ to $1/\sqrt{r}$. Therefore, the fault-normal components are much larger than the fault-parallel components, especially for the buried fault, as shown in Figure 14b. In the vicinity of surface faulting, the combined effects of directivity and fling cause the directions of maximum velocities to become inclined, as shown in Figure 14a. This probably explains the direction of the maximum velocity recorded at Lucerne Valley, as shown in Figure 1b.

Also, we investigated the effects of softer surface layers using the same fault model and found that the softer layers amplify mainly the directivity pulses, but not the fling steps. This is because the body and surface waves of the dynamic Green’s function are excited more strongly in the softer layers than in the static one. In actual situations, however, the existence of softer layers may not only increase the faulting

slip, but also change the slip function itself. The results of dynamic faulting models, laboratory tests, and/or source inversions deduced from strong motion records should be incorporated into future work to model slip functions of surface faults more appropriately.

Finally, we offer the Fortran code of this method for public use. Please contact the first author for information on how to obtain and use the code.

Acknowledgments

This research was partly supported by a special project of U.S. Japan Cooperative Research for Urban Earthquake Disaster Mitigation (no. 11209201), Grant-in-Aid for Scientific Research on Priority Area (Category B), Ministry of Education, Culture, Sports, Science, and Technology of Japan (MEXT), and the Earthquake and Environmental Research Center of Kogakuin University funded by the Frontier Research Promotion Program of MEXT (Y.H.). This work was also supported by the National Science Foundation KDI program, under Grant CMS-9980063 (J.B.); the cognizant program director is Clifford Astill. We are grateful for this support. We obtained the strong motion records used in this study from the PEER Strong Motion Database.

References

Abrahamson, N. (2001). Incorporating effects of near fault tectonic deformation into design ground motions, a presentation sponsored by the Earthquake Engineering Research Institute Visiting Professional Program, hosted by the University at Buffalo, 26 October 2001, <http://mceer.buffalo.edu/outreach/pr/abrahamson.asp>.

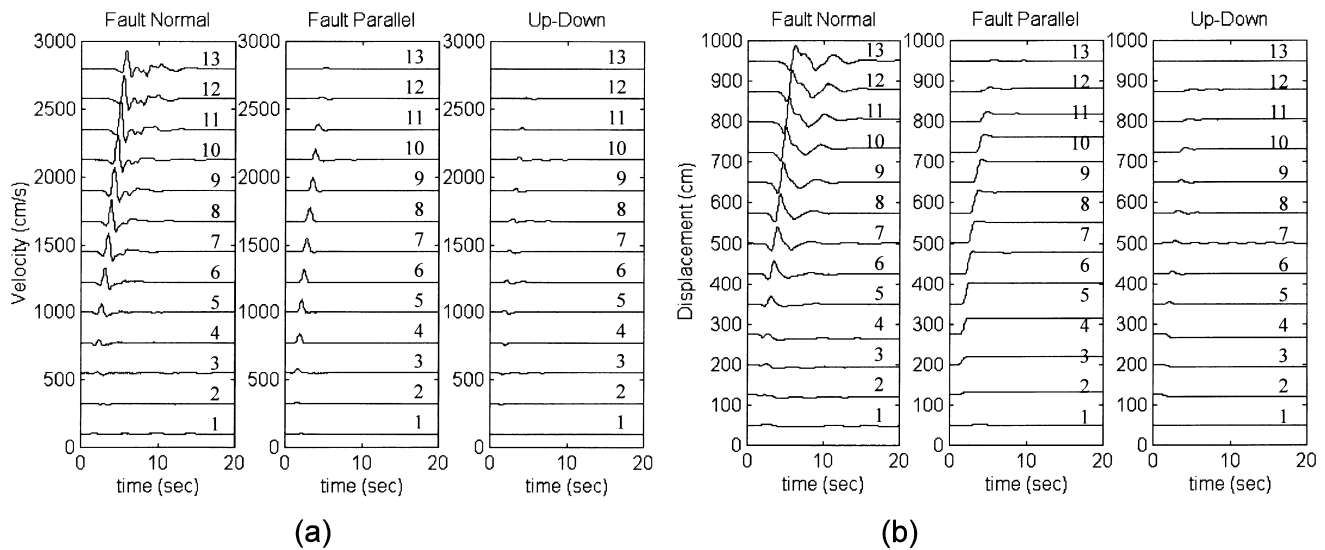


Figure 15. (a) Velocities and (b) displacements using the surface faulting model of Figure 11a in the layered structure, as shown in Table 1.

- Aki, K. (1968). Seismic displacement near a fault, *J. Geophys. Res.* **64**, 321–342.
- Aki, K., and P. G. Richards (1980). *Quantitative Seismology*, Vol. 1, W. H. Freeman, New York.
- Anderson, J. G. (1976). Motions near a shallow rupturing fault: evaluation of the effects due to the free surface, *Geophys. J.* **16**, 575–593.
- Anderson, J. G., and J. E. Luco (1983a). Parametric study of near-field ground motions for strike-slip dislocation models, *Bull. Seism. Soc. Am.* **73**, 23–43.
- Anderson, J. G., and J. E. Luco (1983b). Parametric study of near-field ground motions for oblique-slip and dip-slip dislocation models, *Bull. Seism. Soc. Am.* **73**, 44–57.
- Apsel, R. J., and J. E. Luco (1983). On the Green's functions for a layered half-space. II, *Bull. Seism. Soc. Am.* **73**, 931–951.
- Archuleta, R. J., and G. A. Frazier (1978). Three-dimensional numerical simulation of dynamic faulting in a half-space, *Bull. Seism. Soc. Am.* **68**, 541–572.
- Archuleta, R. J., and S. H. Hartzell (1981). Effects of fault finiteness on near-source ground motion, *Bull. Seism. Soc. Am.* **71**, 939–957.
- Bouchon, M. (1979). Predictability of ground displacement and velocity near an earthquake fault: an example—the Parkfield earthquake of 1966, *J. Geophys. Res.* **84**, 6149–6156.
- Chen, X. (1995). Near-field ground motion from the Landers earthquake. Earthquake Engineering Research Institute, Report 95-02, Caltech, <http://resolver.library.caltech.edu/caltechEERL:1995.EERL-95-02>.
- Colton, D., and R. Kress (1983). *Integral Equation Methods in Scattering Theory*, Wiley, New York.
- Greenfield, R. J. (1995). Comment on “An efficient method for computing Green's functions for a layered half-space with sources and receivers at close depths” by Y. Hisada, *Bull. Seism. Soc. Am.* **85**, 1523–1524.
- Haskell, N. A. (1969). Elastic displacements in the near-field of a propagating fault, *Bull. Seism. Soc. Am.* **59**, 865–908.
- Hisada, Y. (1993). An efficient method for computing Green's functions for a layered half-space with sources and receivers at close depths, I, *Bull. Seism. Soc. Am.* **84**, 1456–1472.
- Hisada, Y. (1995). An efficient method for computing Green's functions for a layered half-space with sources and receivers at close depths, II, *Bull. Seism. Soc. Am.* **85**, 1080–1093.
- Kane, J. H. (1994). *Boundary Element Analysis in Engineering Mechanics*, Prentice Hall, New York.
- Kawasaki, I. (1975). On the dynamic process of the Parkfield earthquake of June 28, 1966, *J. Phys. Earth* **23**, 127–144.
- Kawasaki, I., Y. Suzuki, and R. Sato (1973). Seismic waves due to a shear fault in a semi-infinite medium, I, *J. Phys. Earth* **21**, 251–284.
- Levy, N. A., and K. Mal (1976). Calculation of ground motion in a three-dimensional model of the 1966 Parkfield earthquake, *Bull. Seism. Soc. Am.* **66**, 405–423.
- Luco, J. E., and J. G. Anderson (1983). Steady-state response of an elastic half-space to a moving dislocation of finite width, *Bull. Seism. Soc. Am.* **73**, 1–22.
- Luco, J. E., and R. J. Apsel (1983). On the Green's functions for a layered half-space. I, *Bull. Seism. Soc. Am.* **73**, 909–929.
- Oglesby, D. D., and S. M. Day (2001). Fault geometry and the dynamics of the 1999 Chi-Chi (Taiwan) earthquake, *Bull. Seism. Soc. Am.* **91**, 1099–1111.
- Olver, F. W. J. (1964). Bessel functions of integer order, in *Handbook of Mathematical Functions with Formulas, Graphs, and Mathematical Tables*, Applied Mathematics Series, Vol. 55, M. Abramowitz and I. A. Stegun (Editors), U.S. Department of Commerce, National Bureau of Standards, Washington, D.C.
- Ramacharla, P. K., and K. Meguro (2001). Numerical modeling of dip-slip faults for studying ground surface deformation, *Bull. Earthquake Resistant Structure Research Center* **34**, 107–112.
- Shin, T. C., and T. L. Teng (2001). An overview of the 1999 Chi-Chi, Taiwan, earthquake, *Bull. Seism. Soc. Am.* **91**, 895–913.
- Somerville, P. G., N. F. Smith, R. W. Graves, and N. A. Abrahamson (1997). Modification of empirical strong ground motion attenuation relations to include the amplitude and duration effects of rupture directivity, *Seism. Res. Lett.* **68**, 199–222.

Department of Architecture
Kogakuin University
Nishi-Shinjuku 1-24-2
Tokyo 163-8677, Japan
hisada@cc.kogakuin.ac.jp
(Y.H.)

Department of Civil and Environmental Engineering
Carnegie Mellon University
Pittsburgh, Pennsylvania 15213
jbielak@cmu.edu
(J.B.)